Linking Lattice Strain and Electron Transfer Kinetics in Crystalline Layered Double Hydroxides

Elif Pınar Alsaç[a] and Rodney D. L. Smith[a,b,c]*

[a] Department of Chemistry, University of Waterloo, 200 University Avenue W., Waterloo, Ontario, Canada N2L 3G1

[b] Waterloo Institute for Nanotechnology, University of Waterloo, 200 University Avenue W., Waterloo, Ontario, Canada N2L 3G1

[c] Waterloo Artificial Intelligence Institute, University of Waterloo, 200 University Avenue W., Waterloo, Ontario, Canada N2L 3G1

*Correspondence to:

rodsmith@uwaterloo.ca

ABSTRACT

The improved electrocatalytic properties of disordered metal hydroxides relative to crystalline layered double hydroxides remains a poorly understood phenomenon. We use a hydrothermally synthesized series of mixed metal hydroxides to study these composition-dependent structural similarities and electrochemical behavior differences. X-ray diffraction, X-ray absorption spectroscopy, and Raman spectroscopy provide complementary perspectives on the structure of the $Fe_xNi_{1-x}(OH)_2$ series. These techniques reveal near quantitative incorporation of Fe(III) into the $Ni(OH)_2$ lattice at low Fe-content, but also that Fe(III) is distributed into a contaminating iron oxide phase and a non-traditional coordination environment atop the layered double hydroxide structure as the Fe-content increases. Systematic lattice contraction is observed with increasing Fe-content, similar to structurally disordered analogues, but the electrochemical behavior is markedly different. The characteristic anodic shift of pre-catalytic redox peaks does not occur, and electron transfer kinetics exhibit a much more gradual improvement. Measured Tafel slopes are found to possess a linear relationship with the O-Ni-O bond angles within the lattice across the full composition series. Asymmetric Marcus-Hush theory is used to explain this unexpected result, where Fe(III) ions systematically introduce lattice strain that alters the reaction coordinate for the nickel oxidation reactions.

Keywords: hydrothermal synthesis, lattice strain, electron transfer kinetics, electrocatalysts, iron-nickel hydroxide, Marcus-Hush theory

INTRODUCTION

Iron-doped nickel hydroxides rank as one of the best oxygen evolution reaction (OER) electrocatalysts in alkaline environment and a large range of synthetic protocols have been developed to prepare these materials.[1] Materials exhibiting layered hydroxide type structures can be prepared by pH-induced precipitation,[2,3] anodic electrodeposition,[4–6] cathodic electrodeposition,[7–9] photochemical deposition,[10–13] anodization of metallic electrodes,[14–16] hydrothermal techniques,[17–19] and precipitation in the presence of various small organic molecules.[20,21] Efforts at improving the catalytic properties of this family of materials have focused on tuning morphology[22,23], adding dopants, introducing carbon additives,[24,25] acting as a support for single atoms,[26–28] or using alternative materials such as metal organic frameworks as synthetic precursors.[29] Such a wide variety of fabrication and processing protocols yields variations in overall catalytic performance, but the incorporation of even trace amounts of Fe(III) into $Ni(OH)_2$ type materials consistently yields the same abrupt changes in electrocatalytic response. Structural analyses are commonly performed by a mixture of X-ray diffraction (XRD) and X-ray absorption fine-structure spectroscopy (XAFS), with each approach typically identifying the same minimal set of structural features for all synthetic approaches. With such diversity in synthetic techniques, however, it is highly probable that variations in structural features exist that are hidden behind the abrupt changes in OER activity. Careful analysis of the changes in structure are necessary to identify any such variations, which can be accomplished through structure-property analysis.[30]

Efforts to identify individual coordination environments that are particularly active for electrocatalytic OER have identified several specific structures that may be of importance. The undercoordination of ions residing along the edge, or at corners, of the layered double hydroxide structure are often viewed as the catalytically relevant sites.[31–33] Variations in measurement strategies have revealed unexpected tetrahedrally coordinated sites,[34,35] the ability for elements such as iron and iridium to reside atop the basal plane of $Ni(OH)_2$,[28] systematic variations in iron electronic structure,[4,36,37] the presence of lattice strain due to ionic radius differences between nickel and iron,[10,13] and the possibility of iron redox activity.[38] Analysis using advanced in-operando techniques has yielded some success in identifying sites that may have catalytic relevance.[39–43] Identification of such non-standard sites, however, has been relatively restricted to individual lines of research due to reliance on specialized characterization and analytical

techniques. An understanding of the prevalence of such structural features and the role of synthetic conditions in their effective concentrations will assist in optimizing electrocatalysts performance and stability.

Metal oxyhydroxides synthesized with a hydrothermal route yield more crystalline structures than fabrication techniques such as electrodeposition or co-precipitation.[2,41] Hydrothermally prepared β-$Ni(OH)_2$ provides the highest quality crystals reported to date.[44] Such highly crystalline forms of nickel hydroxide historically serve as alkaline battery cathode materials due to their exceptionally poor ability to catalyze OER; the electrocatalytic capabilities increase dramatically upon introduction of structural disorder.[11,12,45] This change in behavior marks hydrothermally synthesized samples of interest for studying critical structural features through structure-property analysis, particularly if the degree of structural disorder can be systematically affected. Hydrothermal synthesis, however, comes with significant risk of producing contaminating phases such as the spinels Co_3O_4, Fe_3O_4 or $NiFe_2O_4$,[46,47] or disordered platelets as seen in Zn(II) doped aluminum hydroxides.[48] This risk is sufficiently high that phase contamination of layered double hydroxides that are not based on amphoteric ions such as Al(III) has been suggested to be prolific yet underreported in the literature.[49] Phase pure layered double hydroxides can be prepared with the assistance of organic surfactants[50,51] or hydrogen bonding additives such as formamide,[52,53] but this leads to lower crystallinity. A desire to study highly crystalline layered double hydroxides necessitates the use of hydrothermal techniques and associated risk of phase impurity.

We herein report structural and electrocatalytic characteristics of a nominally $Fe_xNi_{1-x}(OH)_2$ composition series fabricated using hydrothermal synthesis. Structural analysis using Raman spectroscopy, XRD, and XAFS show that Fe(III) within $Ni(OH)_2$ yields localized structural distortions, where Ni-sites retain long-range order while Fe-sites show no order beyond *ca.* 3.5 Å. Peaks that emerge in Raman spectra show correlations to structural features that enable Raman spectroscopy to serve as a rapid diagnostic tool. A linear correlation is observed between Tafel slope for OER and bond angles within the material. This behavior deviates from the commonly reported step-wise change in Tafel slope that is commonly reported for iron-nickel hydroxide materials. This trend cannot be explained by the traditional Butler-Volmer model for

electron transfer kinetics, but asymmetric Marcus-Hush theory serves to link the trend to increasing lattice strain with increasing Fe-content.

RESULTS

Powder XRD patterns for the $Fe_xNi_{1-x}(OH)_2$ series are consistent with a well-crystallized structure similar to brucite, with Fe(III) ions inducing structural disorder. All Bragg peaks in the $Ni(OH)_2$ sample can be indexed to the *P-3m1* space group (ICSD: 169978), consistent with β-$Ni(OH)_2$ (Figure 1A).[54] The crystal structure is maintained upon addition of Fe(III) to the reaction flask, albeit with a progressive shrinkage and broadening of Bragg peaks that signify decreased long-range structural order. Neutron diffraction experiments have shown that crystalline β-$Ni(OH)_2$ has a unit cell *a* parameter of 3.1268 Å and a *c* parameter of 4.6060 Å.[55] Successful incorporation of iron ions into the $Ni(OH)_2$ lattice here is confirmed by a monotonic shift in the (100) reflection, which represents M-M distances across di-μ-hydroxo linkages (d_{M-M}). Rietveld refinements show this distance contracts from 3.124 Å for 0% Fe to 3.111 Å for 30% Fe (Figures 1B and S1). The unit cell *c* parameter represents the spacing between 2-dimensional sheets and is static near 4.61 Å until *ca*. 10% Fe content, after which it decreases towards 4.56 Å (Figure 1C). Transmission electron microscopy on the 0, 15 and 30% Fe samples show that the $Fe_xNi_{1-x}(OH)_2$ portion of the sample to exist as *ca*. 20-100 nm hexagonal platelets, in agreement with β-$Ni(OH)_2$,[44,54] while the phase impurity yields denser cubic nanoparticles (Figure S2). Images show no sign of amorphous nature at particle surfaces. The increased disorder and absence of a concerted contraction of both *a* and *c* suggests that iron dopants induce localized distortions in the lattice.

An iron oxide phase contaminant emerges as the amount of iron added to the reaction vessel increases. Bragg peaks at 31, 36, 44, and 57° become visible in the XRD at 10% Fe-content and continually increase in intensity as Fe-content increases (Figure 1A). These peak locations are consistent with the strongest reflections expected for either magnetite[56] (Fe_3O_4; ICSD #49549) or maghemite[57] (γ-Fe_2O_3; ICSD #35643). Due to similarities between the two structures, it is not possible to conclusively identify which is present by XRD; Fe_3O_4 was used for a Rietveld refinements. Rietveld refinements using β-$Ni(OH)_2$ and Fe_3O_4 components provide a measure of the phase fraction of the iron oxide contaminant, confirming that its concentration steadily

increases with Fe-content (Figure 1D). The stoichiometry of iron successfully incorporated into the $Ni(OH)_2$ lattice is therefore not equivalent to the stoichiometry added to the reaction flask, with the observed behavior suggesting that an equilibrium for Fe(III) incorporation into the $Ni(OH)_2$ lattice exists. The largest estimated error in Fe-incorporation within the $Ni(OH)_2$ lattice is *ca*. 1.7% for the 30% Fe sample, a result derived from XAFS results (discussed below), while the remaining estimates are below 1%. We therefore adopt an approximate uncertainty of 1% Fe content as a worst-case scenario for all samples in the series.

Raman spectra on the sample series are consistent with a decrease in long-range order upon Fe-substitution and reveal systematic deprotonation of hydroxyl groups. The brucite structure is expected to yield two A_{1g} and two E_g Raman active modes, but one E_g mode is not observed.[58,59] The pure $Ni(OH)_2$ sample here shows the three commonly observed modes, with an E_g mode at 313 cm^{-1}, an A_{1g} mode at 446 and a second A_{1g} mode at 3580 cm^{-1} (Figure 2A). Incorporation of Fe(III) ions causes the peak for the E_g mode, an antisymmetric movement of oxygen ions on either side of the metal hydroxide layers, to broaden substantially but remain at a static frequency (Figure 2B).[59] The peak for the low frequency A_{1g} mode, a symmetric stretching of M-O bonds, exhibits broadening and an apparent blue shift following incorporation of Fe(III) ions (Figure 2B). The apparent blue shift of this A_{1g} peak may be attributable to the overlap of two poorly resolved bands, evidenced by the clear emergence of a low-frequency peak with a shoulder in the 30% Fe-content sample (Figure 2C). The second A_{1g} mode at 3580 cm^{-1} broadens as Fe-content increases, suggesting deprotonation of hydroxyl groups.[54,60] Such deprotonation is consistent with a strengthening of M-O bonding, as suggested by the observed blue shift of the A_{1g} M-O stretching vibration. Additional O-H vibrations are observed at 3600 and 3687 cm^{-1}. The former is a sharp peak on the high frequency shoulder of the A_{1g} hydroxide stretch that has been previously assigned to surface hydroxide vibrations, while the latter to has been assigned as an A_{2u} O-H stretching vibration that become visible due to disorder in layer stacking.[54]

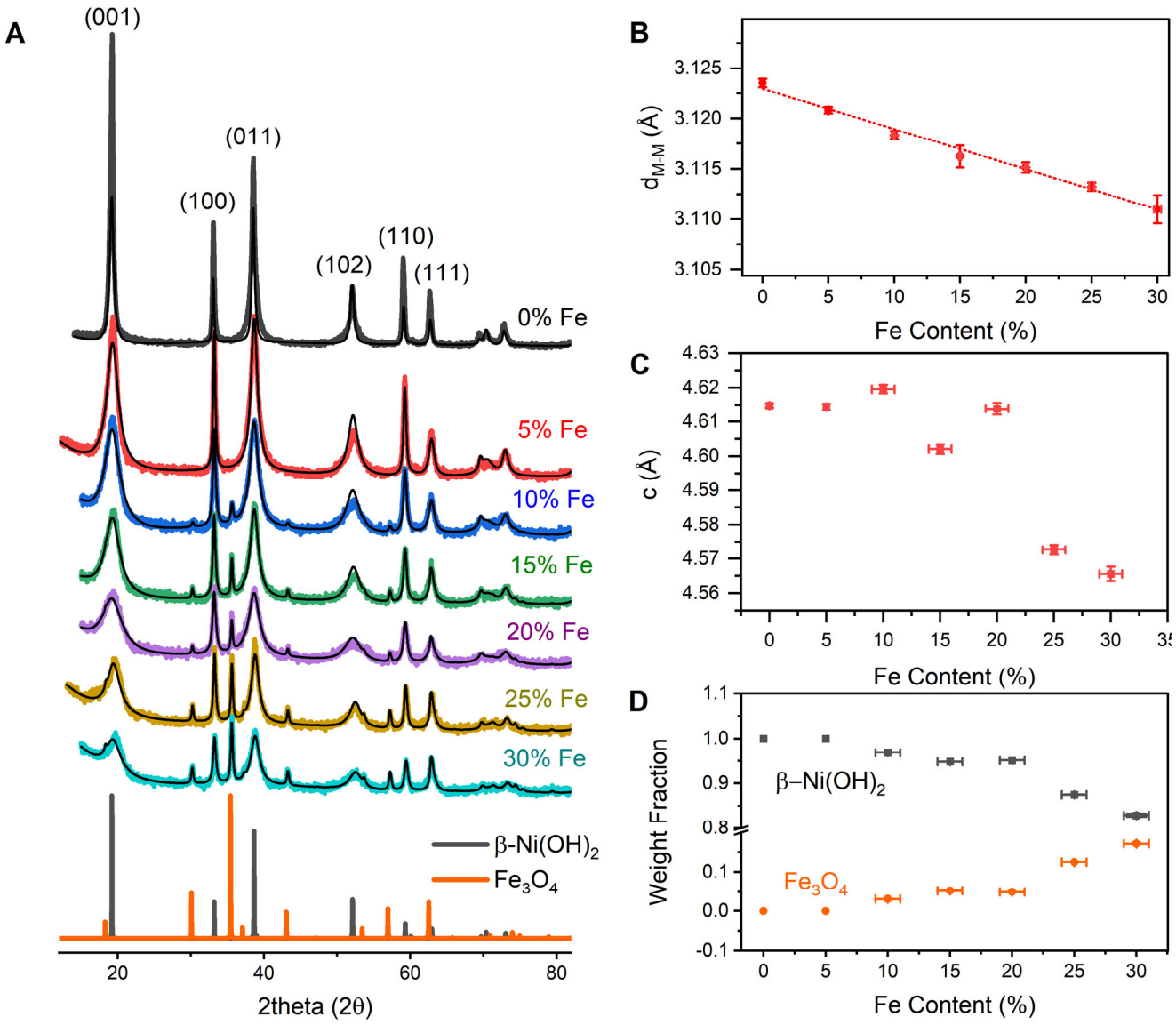

Figure 1: Powder X-ray diffraction analysis of $Fe_xNi_{1-x}(OH)_2$. **(A)** Experimental XRD patterns (data points) and Rietveld refinement fits (lines) for the composition series. **(B)** Composition dependence of the unit cell *a* parameter, which represents metal-metal distances in edge-sharing polyhedra. **(C)** Composition dependence of interlayer spacing. **(D)** Relative weight fractions of β-$Ni(OH)_2$ and magnetite (Fe_3O_4) determined by Rietveld refinement . Errors in Fe content are estimated at 1% for samples with visible phase contamination. Errors in other parameters derived from Rietveld refinements.

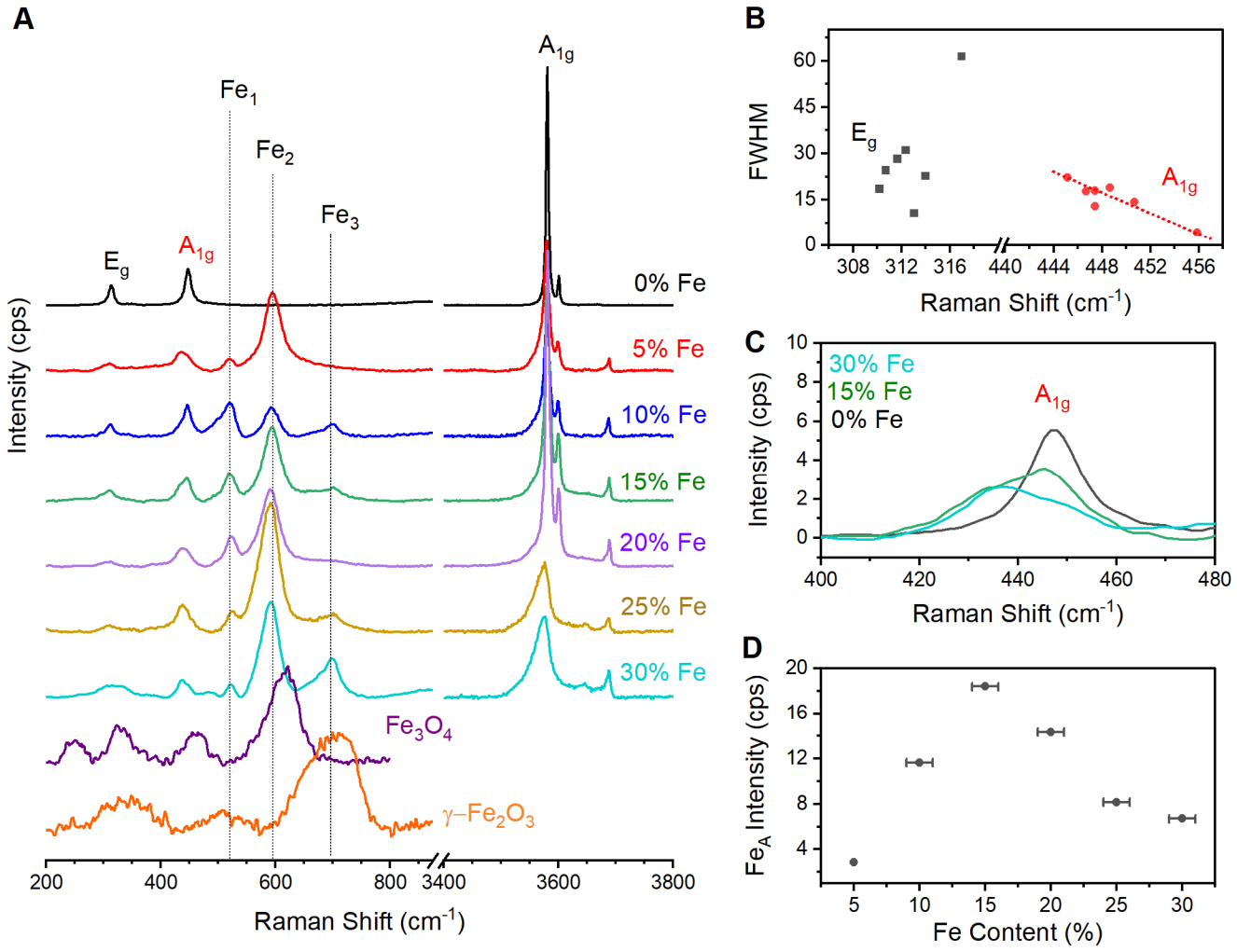

Figure 2: Structural analysis of $Fe_xNi_{1-x}(OH)_2$ with Raman spectroscopy. **(A)** Raman spectra of composition-dependent $Fe_xNi_{1-x}(OH)_2$ series with magnetite and maghemite references. **(B)** Composition dependent Ni-O vibrations. **(C)** Shape evolution of the peak observed for the A_{1g} stretching vibration. **(D)** Composition-dependent intensity of the peak at *ca*. 518 cm^{-1} that is labelled as **Fe_1**. Errors in Fe content are estimated at 1% for samples with visible phase contamination.

The emergence of several additional Raman peaks upon introduction of iron reveals the composition-dependent structural evolution in the material. A peak at *ca*. 518 cm^{-1} (**Fe_1**; Figure 2A) appears immediately upon addition of iron and blue shifts with increased Fe-content. Previous reports indicate that this feature is an M-O stretching mode that arises following substitution of Ni(II) with trivalent cations due to deprotonation.[61] The **Fe_1** peak grows in prominence until 20% Fe before shrinking due to growth of two other peaks, located at *ca.* 600

and 700 cm^{-1}. XRD and XAS (see below) results demonstrate that the proportion of Fe ions successfully incorporated into the $Ni(OH)_2$ lattice is near-quantitative up to 15% Fe content, and a linear trend exists between Fe-content and intensity of **Fe_1** in this composition range (Figure 2D). The intensity of the **Fe_1** feature therefore provides a measure of Fe ions successfully incorporated into the lattice. The peak at *ca*. 600 cm^{-1} (**Fe_2**; Figure 2A) is intense immediately upon addition of Fe to the samples. Past results indicate that the **Fe_2** peak arises in disordered iron-nickel oxyhydroxides due to a second coordination environment for Fe(III) in $Ni(OH)_2$ samples; this coordination environment sits atop the two dimensional $Ni(OH)_2$ sheets.[53] In agreement with the smaller than expected lattice contraction observed in XRD, the intensity of this **Fe_2** Raman peak is significantly greater at low Fe-content values here than previously reported. These secondary sites thus appear more favored for samples prepared by hydrothermal synthesis than for previous alkaline precipitation methods. The final additional peak that emerges upon introduction of Fe is visible at ca. 700 cm^{-1} between 10-30% Fe (**Fe_3**; Figure 2A). The location of this peak is consistent with γ-Fe_2O_3 (Figure 2A),[62,63] which XRD analysis identified as a potential contaminating phase for these compositions.

Composition-dependent changes in the Ni and Fe K-edge X-ray absorption near-edge spectra (XANES) show a distortion of coordination environments. The K-edge spectra for both elements consist of a pre-edge peak and an edge leading to a prominent peak (the “white line”). The former is a symmetry-forbidden electronic transition from 1*s* to 3*d* orbitals while the subsequent edge and peak are the symmetry allowed 1*s* to 4*p* transition.[64–67] The pre-edge peak is stable throughout the composition series in the Ni K-edge spectra (Figure 3A), but increases in intensity in the Fe K-edge spectra as Fe-content increases (Figure 3B). The pre-edge peak in the Fe K-edge data consists of distinct peaks at 7112.2 and 7114.5 eV at low Fe-contents, which is consistent with high spin Fe(III) ions.[64] The two peaks merge into a single, more prominent peak near 7113.3 eV as Fe-content increases. This behavior was also reported for disordered forms of this material where no phase contamination was observed. The pre-edge peak behavior is therefore likely due to greater orbital mixing of the iron 3*d* and oxygen 4*p* orbitals.[64,65,67] The Fe K-edges themselves show evidence of changes in coordination environments. The edge location appears to shift negatively by *ca*. 0.8 eV, which would often be interpreted as a decrease in average oxidation state (Figure 3C, Table S1). The Raman spectra and XRD patterns suggest that γ-Fe_2O_3 or Fe_3O_4 is the contaminant phase, however, suggesting that this apparent shift is

an artefact of a change in either geometry or spin-state. A distinct change in shape of the Fe edge as Fe-content increases supports the assessment that the apparent shift is unlikely a change in oxidation state: (i) the lower portion of the edge increases in intensity to yield an apparent shift towards lower energy, while (ii) the upper portion of the edge decreases in intensity to yield a decrease in white line intensity and an apparent shift towards higher energy (Figure 3B). The Ni edge shows the same behavior, but in a much less pronounced fashion (Figure 3A). The estimated K-edge location shifts negatively by 0.33 eV (Figures 3C), which is also likely to arise due to changes in the coordination environment rather than the nickel oxidation state.

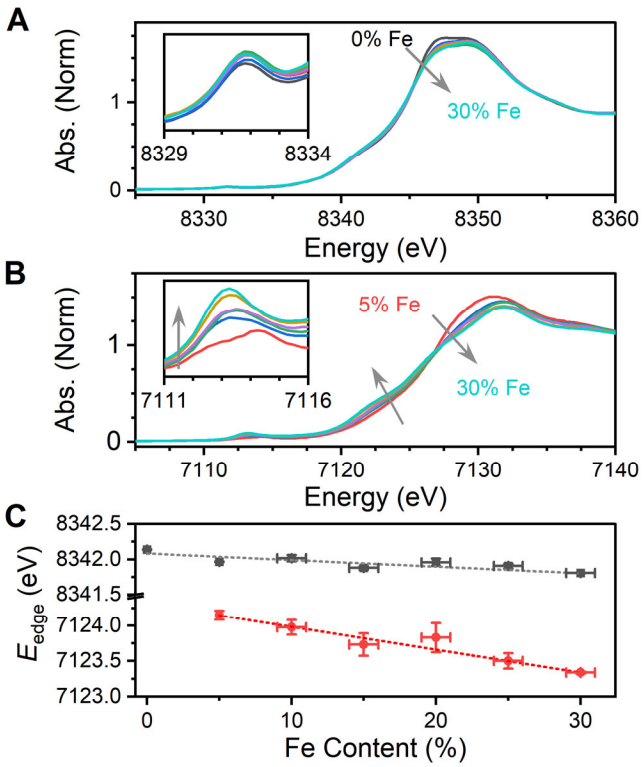

Figure 3: X-ray absorption near-edge spectra for $Fe_xNi_{1-x}(OH)_2$. **(A)** XANES spectra of Ni K-edge of $Fe_xNi_{1-x}(OH)_2$ sample series **(B)** XANES spectra of Fe K-edge of $Fe_xNi_{1-x}(OH)_2$ sample series. **(C)** Composition dependent Ni-K and Fe-K edge locations. Errors in Fe content are estimated at 1% for samples with visible phase contamination. Errors in K-edge location are the standard deviation of at least 3 independent spectra.

Wavelet transform (WT) analysis appears capable of revealing the iron oxide phase contamination, but not differentiating between Ni and Fe ions residing within the $Ni(OH)_2$ lattice.

WT offers improved resolution of scattering paths when *R*-values are similar but oscillations are present in different *k*-space.[68,69] The strongest features in WT of k^3-weighted data are maxima corresponding to M-O and edge-sharing M-M shells (Figure 4). The M-O shells predominantly reside in the low-*k* portion of the data, while the M-M shell resides in the mid-*k* region. The intensity of the Ni-M feature decreases as Fe-content increases, which is consistent with disorder arising from increased variation of bond distances. The Fe-M feature is instead very weak at low Fe-content and increases with Fe-content in the samples (Figures 4D-F). This growth shows two features that are separated in both *k*-space and *R*-space and are not observed in the Ni K-edge data, confirming the addition of at least two new Fe-M coordination shells.[33] This perspective on the data shows that the increased structural disorder in the nickel sites of $Fe_xNi_{1-x}(OH)_2$ samples arises due to fundamentally different structural modifications than in the Fe sites.

Extended X-ray absorption fine-structure spectra (EXAFS) confirm the differences in the Fe and Ni coordination environments and provide a secondary quantitative measure of iron distribution. Fourier-transforms of k^3 weighted data for the Ni K-edge show the features expected for a well-defined layered double hydroxide (Figure 5A, Table S2): peaks at reduced *R* values near 1.85 and 2.90 Å correspond to Ni-O and Ni-M coordination shells. A peak at *ca.* 6 Å is the third M-M distance within the $Ni(OH)_2$ lattice, and the feature near 4 Å is a multi-leg path.[10,70] These features are only observable in $Ni(OH)_2$ samples that exhibit substantial long-range order. The element specificity of EXAFS enables $R_{Ni\text{-}O}$ and $R_{Ni\text{-}M}$ to capture only the Ni ions within $Fe_xNi_{1-x}(OH)_2$, providing a complimentary perspective to the average of Fe and Ni ions measured by XRD ($d_{M\text{-}M}$). The Fe K-edge data contains the first Fe-O and Fe-M peaks but is notably missing all of the higher distance features, even for the 5% Fe which contains no observable phase contamination (Figure 5B, Table S3-4). The observation of measurable long-range order in the Ni environments but not the Fe environments demonstrates that Fe ions successfully incorporated into $Ni(OH)_2$ induce distortions that are highly localized within the lattice.

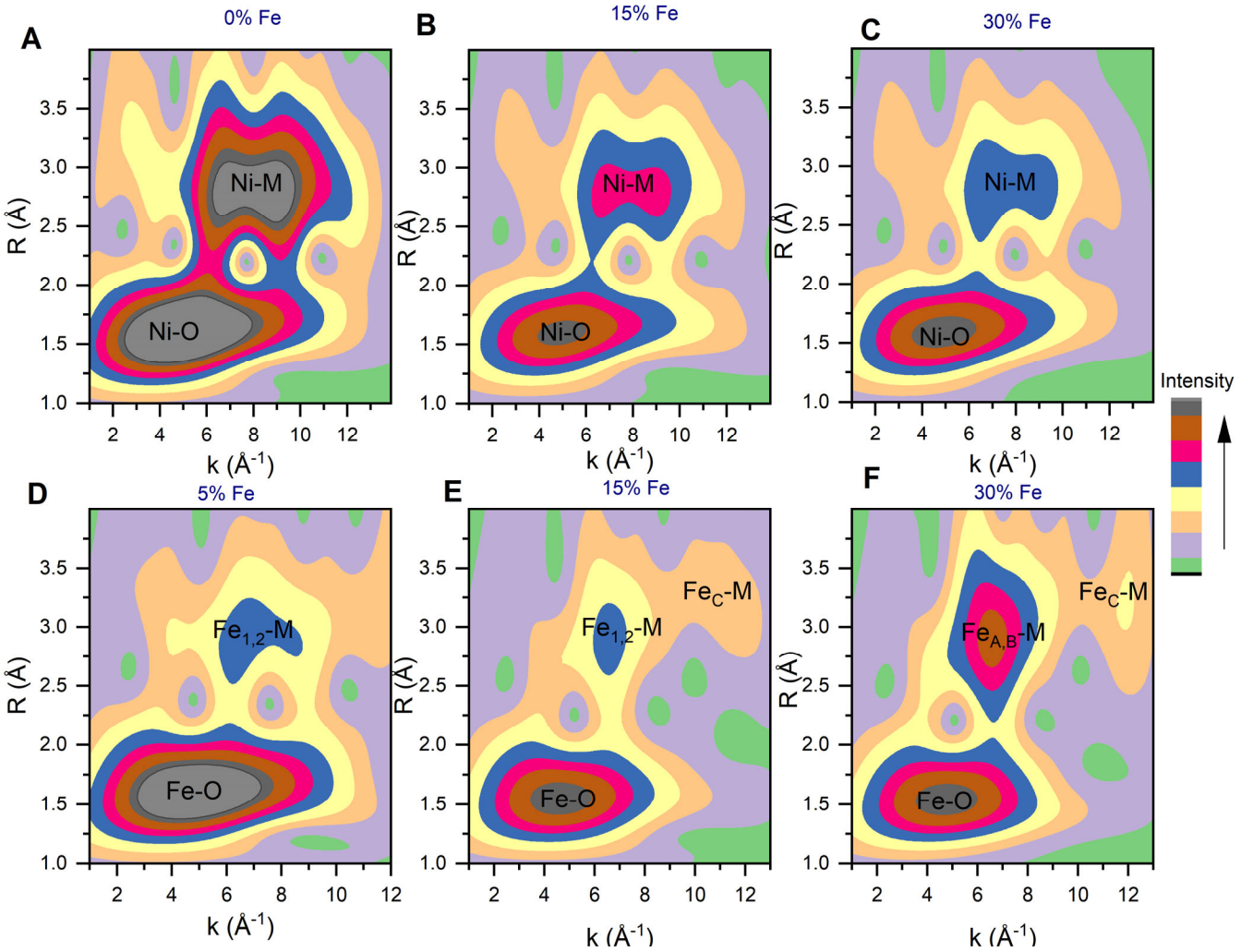

Figure 4: Wavelet transform analysis of $Fe_xNi_{1-x}(OH)_2$. Continuous wavelet transforms performed using a Morlet wavelet on k^3 weighted data for the Ni K-edge in **(A)** 0% Fe **(B)** 15% Fe **(C)** 30% Fe, and for the Fe K-edge in **(D)** 5% Fe **(E)** 15% Fe **(F)** 30% Fe.

Simulation of Ni K-edge EXAFS data provides a secondary means to quantify phase contamination across the sample series. The $R_{Ni\text{-}M}$ shell decreases from 3.13 to 3.11 Å as Fe content increases, consistent with XRD trends (Figure 1), but the $R_{Ni\text{-}O}$ distance remains constant near 2.07 Å (Figures 5C and 5D). The Fe K-edge data is more complex due to phase contamination, with the Fe-M shell near 3 Å splitting into multiple features at 10% Fe content. Simulation of the Fe data using the brucite and magnetite crystal structures simultaneously enables a form of linear combination analysis. The most prominent shells expected for each crystalline material present were selected and their coordination numbers linked according to

the expected crystalline stoichiometry. The coordination numbers for the octahedrally coordinated M-O shells in each of the two structures were then linked to each other, with the restriction that they sum to 6.0 between the two crystal structures. A direct measure of the weighted average of each crystal structure within the material can then be obtained through the relative coordination numbers between these octahedral shells; the Fe-M shells were similarly analyzed and found to yield consistent results. Coordination numbers are highly correlated to both the amplitude reduction factor and the Debye-Waller factors, so both were fixed for all samples. Simulations on the Fe sites show a coordination number of 6.0 for the $M(OH)_2$ structure, confirming the XRD, Raman spectroscopy and WT judgements that 5% Fe contains no detectable phase contamination. This coordination number gradually decreases to 4.5 for 30% iron content due to the formation of the contaminating phase (Figure 5E). The weighted average values can serve to quantify the amount of Fe that is successfully incorporated into the $Ni(OH)_2$ lattice (Figure 5E).

Comparisons of bond distances from the EXAFS simulations support the assertion that Fe ions induce highly localized distortions. The M-O and M-M distances are consistent between the Fe and Ni K-edge data only for the 5% Fe sample. Clear and strong trends in bond distances are observed for Fe ions within the $Ni(OH)_2$ lattice, with $R_{Ni\text{-}O}$ decreasing from 2.02 Å to 1.95 Å and $R_{Ni\text{-}M}$ decreasing from 3.12 to 3.06 Å. These values signify a large deviation from those in the Ni K-edge data. This is consistent with Fe ions inducing highly localized strain within the lattice. The distances between Fe atoms within the contaminating phase show only minor variations (Figure 5F), which both supports the validity of the linear combination component analysis approach and indicates that the contaminant is not intimately interfaced with the nickel hydroxide lattice.

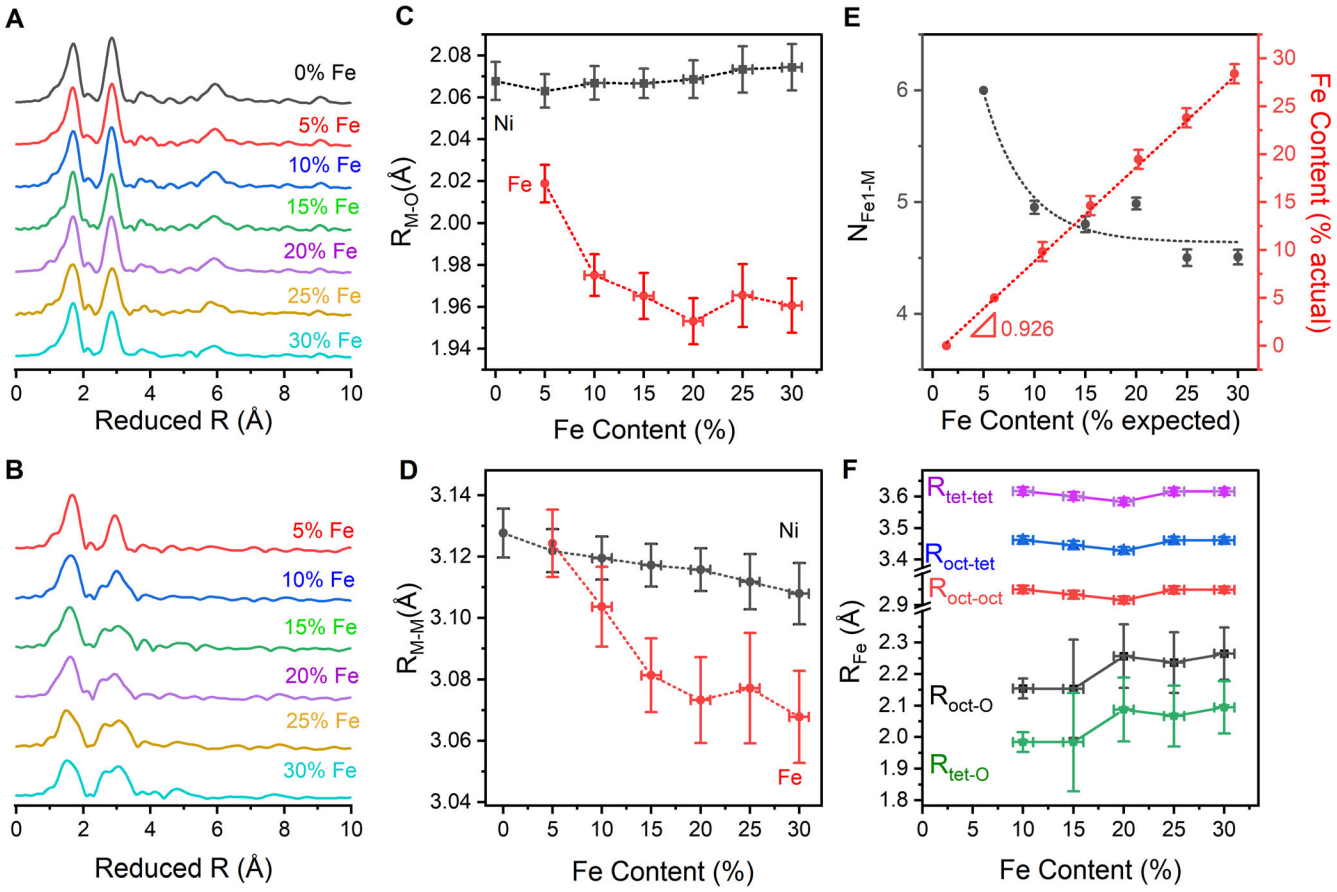

Figure 5: Fourier transformed EXAFS spectra of the **(A)** Ni K-edge and **(B)** Fe K-edge. Composition dependent changes in **(C)** M-O bond lengths and **(D)** M-M bond lengths for ions within the $Ni(OH)_2$ lattice. **(E)** Composition dependent coordination numbers (N) of nickel hydroxide and comparison between the theoretical and measured Fe-content within the $Ni(OH)_2$ lattice. **(F)** Composition dependent bond distances of magnetite phase. Errors in Fe content are estimated at 1% for samples with visible phase contamination. Errors in all EXAFS parameters were estimated using Artemis software package.

Cyclic voltammograms of the composition series are qualitatively comparable to commonly reported behavior, but notable quantitative differences exist. Voltammograms contain a single set of pre-catalytic Faradaic peaks (Figure 6A). Structurally disordered iron-nickel hydroxide samples, such as those synthesized by anodic electrodeposition, aqueous precipitation, or photochemical decomposition, exhibit systematic anodic shift of *ca*. 2.5 mV per percent Fe for both the anodic and cathodic peaks upon Fe incorporation.[8,10,13,71] Such a shift is not observed in the hydrothermally prepared sample series here (Figure 6A). These Faradaic peaks instead broaden and distort but remain approximately static with a half-peak potential of 1.38 V vs. RHE.

The electrocatalytic OER capabilities of the sample series are also different, revealing a smooth composition-dependent trend rather than the frequently reported abrupt change.[10,13,72] Semi-logarithmic current-potential plots (i.e., Tafel plots) for all samples show the linear behavior indicative of kinetically limited electron transfer reactions (Figure S3). The Tafel slope for the 0% Fe sample is measured to be 70 mV dec^{-1}, with the value linearly decreasing towards 33 mV dec^{-1} for 30% Fe (Figure 6B). Onset overpotentials, defined here as the potential where linearity begins in semi-logarithmic Tafel plots, show a similar linear trend, steadily decreasing from 0.2 to 0.1 V (Figure 6C). These more defined electrokinetic parameters offer a potential means to resolve structural features responsible for the classically observed decrease in Tafel slope.

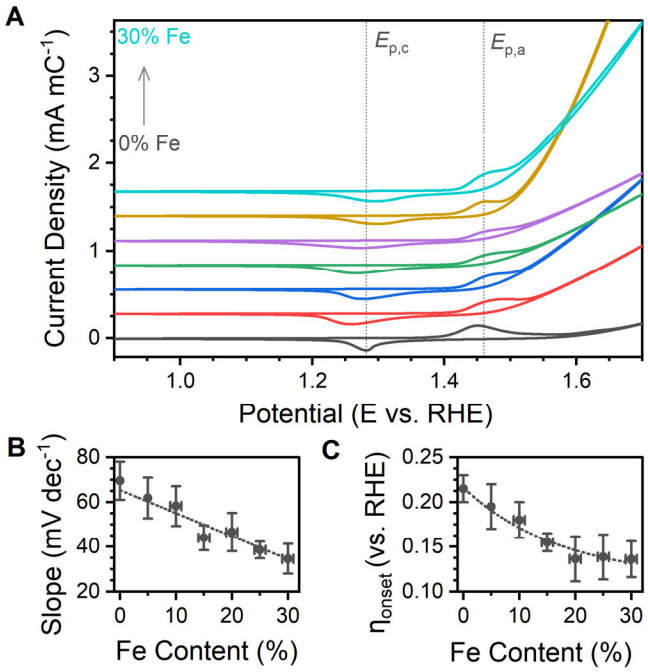

Figure 6: Electrochemical behavior of $Fe_xNi_{1-x}(OH)_2$. **(A)** Cyclic voltammograms acquired at 10 mV s^{-1} on $Fe_xNi_{1-x}(OH)_2$. Composition dependent trends in **(B)** Tafel slopes **(C)** onset overpotentials. Tafel slopes are given as the average between distinct electrodes and error bars represent their standard deviation. All experiments were performed in 1 M KOH electrolyte solutions. Errors in Fe content are estimated at 1% for samples with visible phase contamination. Errors in electrochemical parameters represent the standard deviation of at least two independent measurements.

DISCUSSION

Multiple complementary techniques indicate successful incorporation of Fe(III) ions into the $Ni(OH)_2$ lattice while also providing evidence for ions in secondary phases and coordination environments. Powder XRD confirms that a single contaminating phase, attributable to γ-Fe_2O_3, appears at 10% Fe and grows in prevalence as nominal Fe-content increases (Figure 1D). Raman spectra for the sample series contain three composition-dependent peaks that are consistent with expectations for the $Ni(OH)_2$ lattice (Figure 2).[54,61] Three distinct peaks become prominent after iron is introduced: a peak at ca. 500 cm^{-1} that is assigned as M-O stretching following deprotonation (**Fe$_1$**; Figure 2),[61] a peak at ca. 700 cm^{-1} that identifies the phase impurity as γ-Fe_2O_3 (**Fe$_3$**; Figure 2),[63,73] and a peak at *ca*. 600 cm^{-1} (**Fe$_2$**; Figure 2). This third peak has been variably assigned as a second-harmonic of the E_g mode at *ca*. 300 cm^{-1},[54] to the presence of cation vacancies,[74] and to Fe(III) ions residing in a coordination environment atop the 2-dimensional sheets within $Ni(OH)_2$.[53] Assignment as a second-harmonic is unlikely here because the peak is an order of magnitude more intense than the fundamental E_g mode and increases in intensity with Fe-content and associated structural disorder. The use of hydrothermal synthetic protocol, which is known to yield high quality crystallites,[1,2,75] and the quality of Rietveld refinements using cation occupancy values of unity similarly rule out that cation vacancies exist at a concentration necessary to yield the magnitude of peak in the Raman spectra. We therefore assign the Raman vibration at *ca*. 600 cm^{-1} to the presence of Fe(III) ions residing atop $Ni(OH)_2$ sheets that are linked in an edge-sharing fashion. The Fe(III) ions used during synthesis are therefore distributed across three identified locations.

An upper bound for the stoichiometry of iron ions successfully incorporated into the $Ni(OH)_2$ lattice can be established. The phase fraction of the two crystalline species obtained by Rietveld refinement provides a measure of the distribution of Fe(III) ions between these phases (**Fe$_1$** and **Fe$_3$**), which enables calculation of Fe(III) ions successfully incorporated into the $Ni(OH)_2$ lattice (Figure 7A). This approach suggests that the real stoichiometry is slightly lower than the nominal concentration (e.g., 29.7% measured vs. 30% nominal). A secondary estimate of the real stoichiometry can be obtained by a restricted simulation of EXAFS results to accomplish a linear combination analysis (Figure 5). This approach provides values that are consistent, albeit slightly lower (*e.g.*, 28.40% measured vs. 30% nominal) than the values provided by XRD (Figure 7A). The calculations to derive these values include only Fe(III) ions within either $Fe_yNi_{1-y}(OH)_2$ or the

phase contaminant (i.e., Fe_1 and Fe_3 sites). An inability to quantitatively measure the number of Fe(III) ions in the secondary site (**Fe_2**) by EXAFS or XRD means that these values are an overestimation.

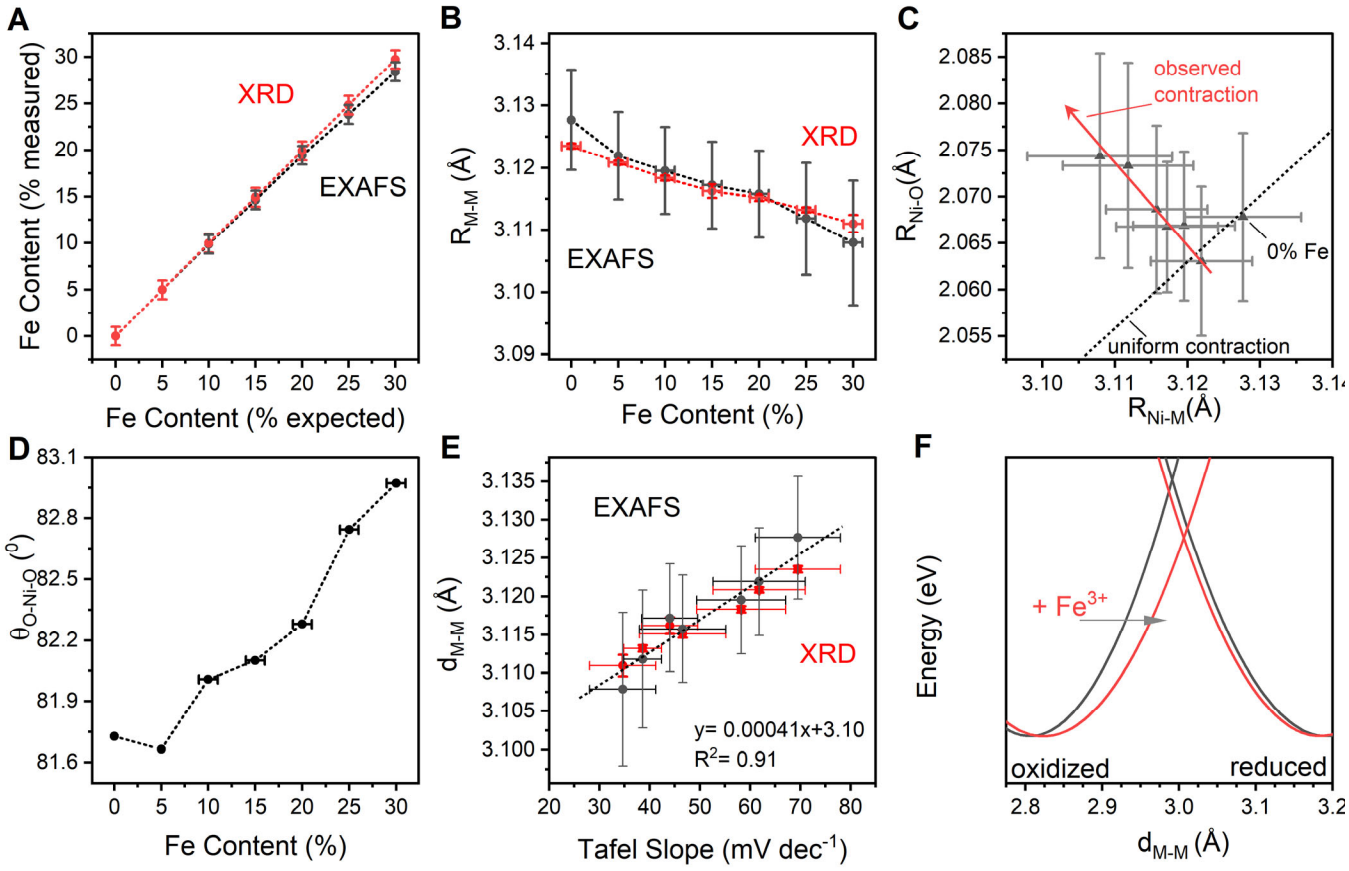

Figure 7: Correlational analysis with different characterization techniques. **(A)** Actual Fe content versus those measured by Rietveld refinement and EXAFS simulation. **(B)** Comparison of d_{M-M} measured by Rietveld refinement of XRD results with R_{Ni-M} determined by EXAFS simulations. **(C)** Relationship between R_{Ni-M} and R_{Ni-O} obtained from EXAFS. The linear slope of 0.67 designates the values necessary for uniform expansion or contraction of the crystal lattice. **(D)** Dependence of O-M-O angles for edge-sharing Ni-M coordination environments. **(E)** Correlation between $\mathbf{d}_{M-M}$, measured by XRD, and $\mathbf{R}_{Ni-M}$, measured by EXAFS simulations, with Tafel slope for OER. **(F)** Potential energy surfaces of $Ni(OH)_2$ and $Fe_xNi_{1-x}(OH)_2$.

Composition dependent structural changes measured by XRD and EXAFS indicate that Fe(III) induces a non-uniform structural compression of $Ni(OH)_2$. The metal-metal distance across di-μ-hydroxo linkages can be directly measured as the unit cell *a* parameter by XRD (d_{M-M}) and as the second coordination shell in EXAFS (R_{Ni-M}). These two measures are in excellent agreement

with each other, both showing a linear contraction of 0.02 Å across the series (Figure 7B). This contraction corresponds to compressive strain of 0.6%, but contraction of the lattice upon electrochemical oxidation of Ni sites has been shown to invert this to tensile strain and amplify its magnitude.[10,13] The magnitude of contraction is notably smaller than for samples prepared by synthetic protocols that exhibit greater structural disorder, which showed a linear contraction of nearly 0.07 Å up to 21% Fe.[10,76] Uniform contraction of the crystal lattice would necessitate a concerted decrease in these di-μ-hydroxo motifs and in Ni-O distances, but Ni-O bond distances measured by EXAFS are consistent across the composition series (Figure 5C). Direct comparison of $R_{Ni\text{-}O}$ to $R_{Ni\text{-}M}$ reveals a trend (Figure 7C) that is only possible if the coordination environments are progressively distorted with increased Fe-content. The element specificity of EXAFS-derived $R_{Ni\text{-}O}$ and $R_{Ni\text{-}M}$ values enable calculation of O-Ni-O bond angles within the 2-dimensional $Fe_xNi_{1-x}(OH)_2$ sheets (see Supplementary Information), which reveals that the lattice distortion involves increased bond angles (Figure 7D).[10,77]

While the composition dependent structural features in this sample series are qualitatively comparable to those frequently reported in the literature, their effect on electrochemical behavior is notably different. The two most prominent changes in electrochemical behavior commonly reported for Fe(III)-doped $Ni(OH)_2$ are an anodic shift in the pre-catalytic redox peaks and a stepped decrease in Tafel slope for electrocatalytic OER. The shift in redox peak has been documented for sample series prepared by anodic electrodeposition,[71] cathodic electrodeposition,[22] and photodeposition,[10,13] occurring at a rate of ca. 2-4 mV per percent Fe added, but appears somewhat dependent on fabrication protocol.[78] In the present study, this peak differs by showing remarkable stability. The second expected change is a strong decrease in Tafel slope towards *ca*. 30 mV dec^{-1}, which has been shown to occur even by simple exposure to Fe(III) impurities in the electrolyte solution at a parts-per-billion levels.[79,80] Existing reports show this transition to be essentially an on-off switch, providing little means to study the transition in detail. In the present study, the Tafel slope is found to linearly decrease as a function of metal-metal spacing across di-μ-hydroxo linkages (Figure 7E); because $d_{M\text{-}M}$ and the O-M-O bond angles are themselves linearly correlated, this relationship also links Tafel slope to bond angle changes. This relationship is not compatible with traditional microkinetic analyses of electron transfer reactions, which relate a static Tafel slope to a rate limiting step.[81–83] A more advanced model of electron transfer kinetics is required to understand this behavior.

Observed trends in structure and behavior suggest that the electrochemical behavior changes are induced by successful incorporation of Fe into the Ni lattice and not the phase impurity. The impurity may introduce a heterojunction or change the identity of active sites, but a sudden change in catalytic mechanism or kinetics for the rate limiting step would be expected for such changes. Following Butler-Volmer theory, such a change would result in a sudden change in Tafel slope rather than the smooth gradient observed in Figure 7E.[82,83] Further, both Fe_3O_4 and γ-Fe_2O_3 are not known to be effective OER catalysts. A change in surface area would result in an error in current density calculations; this error would affect all points uniformly and therefore not affect the Tafel slope. A decrease in conductivity would distort the potential axis such that Tafel plots distort away from ideal linearity, but all plots analyzed are clearly linear (Figure S3). The strong correlation of Tafel slope with both bond angles and bond distances within the $Fe_xNi_{1-x}(OH)_2$ can therefore be attributed to changes in bonding structure of the electrocatalyst.

The observed linear trends in Tafel slope necessitate that Fe incorporation yields a systematic change in the shapes of the potential energy surfaces (PES) for the anodic and cathodic forms of the catalyst. The Butler-Volmer formalism, which oversimplifies the PES landscape by approximating all to be linear, captures the influence of PES symmetry on electron transfer kinetics through the transfer coefficient (α). This empirical fraction is generally assumed to be 0.5 in the heterogeneous electrocatalysis literature, but α is a fraction that can exist above 0 and below 1.0. Studies on molecular systems suggest that the parameter is associated with structural reorganization following electron transfer reactions and values spanning at least 0.3 to 0.7 have been documented.[84–88] Asymmetric Marcus-Hush theory has emerged as a more complex, but physically meaningful model. This approach uses a more realistic parabolic shape for potential energy surfaces (PES) such that the original α parameter can be explicitly defined as:

$$\alpha(E) = \frac{1}{2} + \gamma\left(\frac{1}{4} - \frac{1.267}{\Lambda+3.353}\right) \quad (1)$$

Where Λ is the reorganization energy from Marcus-Hush theory and γ is a fraction representing the relative shape of the two parabolic PES.[86–89] A broader PES surface for the oxidized state relative to the reduced state, which DFT calculations have predicted following Fe-doping of $Ni(OH)_2$,[13] would yield a negative value for γ that would decrease α and the observed Tafel slope for OER. We therefore attribute the observed linear decrease in Tafel slope to a systematic

increase in lattice strain as Fe-content increases. This provides a viable explanation for the observed differences between ordered and disordered $Fe_xNi_{1-x}(OH)_2$ sample series: the localized nature of lattice strain induced by Fe(III) ions observed here means that this strain is not experienced by most nickel centers in well-crystallized materials – the smaller platelet size in disordered phases makes strain effects more prominent at much lower Fe(III) concentrations. These results are of interest to the electrocatalysis community because they identify a practical system that can be used to explore the utility of asymmetric Marcus-Hush theory in electrokinetic analyses in solid-state electrochemistry. This capability can serve to harmonize research efforts on strain engineering[90,91] with those on fundamental electron transfer theories.

CONCLUSIONS

A hydrothermal approach was used to fabricate a well-crystallized composition series of $Fe_xNi_{1-x}(OH)_2$, which exhibited similar structural features to their commonly reported disordered counterparts but different electrochemical behavior. Raman spectroscopy, XRD and XAS revealed that the majority of Fe(III) ions were successfully incorporated within the $Ni(OH)_2$ framework, with minor distribution into an iron oxide phase impurity and a secondary coordination site atop the 2-dimensional $Ni(OH)_2$ framework. Qualitatively similar composition-dependent changes in structure and electrochemical characteristics were similar to those commonly reported for disordered forms of $Fe_xNi_{1-x}(OH)_2$ but were markedly different in a quantitative sense. The pre-catalytic redox peak showed little movement following Fe(III) incorporation and, more importantly, the Tafel slope showed a linear decrease with respect to both M-M spacing and to O-Ni-O bond angles. This unexpected behavior is rationalized using asymmetric Marcus-Hush theory, where lattice strain induced by Fe(III) ions alters the relative symmetry of potential energy surfaces for the oxidized and reduced states of the material. These results identify a system that is of interest for advancing more complex theories of electron transfer kinetics in solid state materials while simultaneously rationalizing the significant differences in behavior between well-crystallized and disordered forms of $Fe_xNi_{1-x}(OH)_2$.

EXPERIMENTAL

Materials. Nickel chloride hexahydrate ($NiCl_2.6H_2O$) (Fisher Chemical), ferric chloride ($FeCl_3$) (Fisher Chemical), sodium hydroxide, and potassium hydroxide (NaOH and KOH) (Sigma-Aldrich) were used as received. All H_2O used during fabrication was milli-Q H_2O (18.2M Ω).

Hydrothermal Synthesis. A total metal concentration of 0.6 M of appropriate amounts of nickel chloride hexahydrate and ferric chloride and 40 ml solution of 5 M potassium hydroxide is added into a Teflon autoclave. The reactor was first heated to 140 ^{0}C with 5 ^{0}C increments and held for 16 hours. Then, the supernatant is removed, and solid particles were washed with Milli-Q water and added into an autoclave with 40 ml of Milli-Q water and heated to 170 ^{0}C with 10-degree increments and held for 16 hours. The final product is vacuum filtrated and rinsed with water and ethanol. Powder products were obtained after samples were dried in an oven at 200 ˚C for two hours.

Electrochemical Experiments. A Biologic SP-300 potentiostat was used for all the electrochemical experiments. Experiments were conducted in a single compartment polyethylene cell containing 1 M KOH electrolyte solution. A Gaskatel HydroFlex reversible hydrogen electrode (RHE) as reference electrode, platinum mesh as the counter electrode, and Toray carbon fiber paper was used as a substrate for the working electrode. Cell resistances were recorded with impedance spectroscopy at the beginning of each experiment, the values were on the order of 5 Ohms for all the samples. Cyclic voltammetry experiments were recorded between 0.9 and 1.7 V vs RHE electrode at 10 mV sec^{-1} scan rate with ten cycles, and the last cycle of each sample was compared. All currents are normalized by charge passed under the cathodic redox peak in cyclic voltammogram.[53,92] This normalizes electrochemical results relative to the number of electroactive nickel centers, which accommodates unavoidable variations in sample loading, ohmic contact between sample and the electrode, changes in sample morphology, or changes in accessibility of redox active sites to electrolyte solution on the timescale of the experiments. Cyclic voltammetric results showing normalization by geometric surface area are provided (Figure S4). Electrokinetic parameters were extracted from chronoamperometry experiments. Chronoamperometry experiments were recorded in both anodic and cathodic directions between 0.9 V and 1.7 V in 10 mV and one-minute steps and

Tafel slopes were calculated from cathodic directions of each sample. All voltages are reported with respect to the RHE scale unless otherwise stated.

Electrode Preparation. A suspension of 5 mg of catalysts, 780 µL of ethanol, 200 µL of water, 20 µL of 0.5% Nafion®, and ca. 0.25 mg of carbon black were sonicated, and 30 µL of this solution was dropped onto carbon fiber paper. The electrodes were dried at room temperature overnight.

X-Ray Absorption Spectroscopy. XAS experiments were performed at the Beamline for Materials Measurement (BMM) at the National Synchrotron Lights Source II (Brookhaven National Laboratory, NY, USA) using a Si(111) monochromator. Data were collected in transmission mode for the Ni K-edge of all samples, and in both transmission and fluorescence mode (4 element Si drift detector) for Fe K-edge data. The Athena software package was used for standard baseline subtraction and normalization of XAS spectra.[93] The K-edge locations were determined by applying the half-height method to the normalized spectra. The Artemis software package was used to generate structural models by simulation of k^3 weighted EXAFS results from k of 3 to 15 $Å^{-1}$ and 3 to 13 $Å^{-1}$ for Ni K- edge and Fe K edge respectively (Figures S4-S5). imulations were performed with an amplitude reduction factor of 0.8 for all samples. A fixed coordination number (N_i) of 6 was used for Ni-M and Ni-O shells. Coordination numbers of Fe shells were allowed to vary, with the sum of octahedrally coordinatated Fe-O shells for the layered double hydroxide and Fe_3O_4 phases fixed to 6. The remaining Fe-centered coordination shells within the Fe_3O_4 phase were defined relative to this constrained shell using ratios expected in the crystal structure (Table S4). The Debye-Waller factor (σ^2) was fixed at 0.006 $Å^2$ for nickel and 0.004 $Å^2$ for oxygen shells. The σ^2 values for Fe shells are 0.011 and 0.007 for layered double hydroxide and 0.002 and 0.0035 for magnetite Fe-M and Fe-O shells respectively. A constant value of E_o is used for Ni 8113 eV and iron 7112 eV. MorletE program is used for Wavelet transform (WT) analysis.[94] In WT expression η and σ are two adjustable parameters for the resolution of spectra. Typically, $\eta \cdot \sigma = 2R$ where R is the magnitude of the region of interest in the R-space. We used 30 for η and 0.2 for σ following the values in the literature.[95] The k-ranges are 1-14 $Å^{-1}$ for Ni K-edge and 1-12 $Å^{-1}$ for Fe K-edge. The R-ranges are between 1-4 Å for both edges.

X-Ray Diffraction. A PANalytical Empyrean diffractometer was used for X-Ray diffraction experiments with Cu Ka radiation (λ = 1.5405 Å) and 2θ angles between 10-80 degrees at a step size of 0.0250. The Bragg–Brentano geometry equipped with a PIXcel bidimensional detector with a Ni Kβ filter was used. Rietveld refinements are done with GSAS-II software.

Raman Spectroscopy. Measurements were performed using a Renishaw inVia Reflex confocal Raman microscope. A 532 nm (Renishaw DPSSL laser, 50 mW) laser, filtered to 1% of maximum intensity, was used in conjunction with 1800 lines/mm diffraction grating. Raman data were processed and analyzed by Renishaw WiRE 5.3 software package. Processing of spectra includes subtraction of baseline, spectrum normalization, and curve fitting.

CONFLICTS OF INTEREST

There are no conflicts to declare.

ASSOCIATED CONTENT

Electronic supplementary information is available. Tabulated parameters extracted from XANES and EXAFS results, complete EXAFS results in *k*-space, complete Tafel plots, CVs, TEM images and phase composition and bond angle calculations.

ACKNOWLEDGEMENTS

We thank the Natural Sciences and Engineering Research Council (NSERC) for support of this project through the Discovery Grants program, and the Canada Foundation for Innovation for infrastructure funding. This document was prepared by the University of Waterloo as a result of the use of facilities of the U.S. Department of Energy (DOE), which are managed by Brookhaven Science Associates, LLC, acting under Contract No. DE-SC0012704. Neither Brookhaven Science Associates, LLC, DOE, the U.S. Government, nor any person acting on their behalf: (a) make any warranty or representation, express or implied, with respect to the information contained in this document; or (b) assume any liabilities with respect to the use of, or damages resulting from the use of any information contained in the document. The authors thank X. V. Medvedeva for acquiring TEM images.

REFERENCES

(1) Karmakar, A.; Karthick, K.; Sankar, S. S.; Kumaravel, S.; Madhu, R.; Kundu, S. A Vast Exploration of Improvising Synthetic Strategies for Enhancing the OER Kinetics of LDH Structures: A Review. *J. Mater. Chem. A* **2021**, *9* (3), 1314–1352. https://doi.org/10.1039/D0TA09788H.

(2) Rong, W.; Stepan, S.; Smith, R. D. L. Evidence of Variations in Atomic Distribution in Disordered Mixed Metal Hydroxides. *MRS Advances* **2019**, *4* (33–34), 1843–1850. https://doi.org/10.1557/adv.2019.325.

(3) Ramesh, T. N.; Kamath, P. V. Synthesis of Nickel Hydroxide: Effect of Precipitation Conditions on Phase Selectivity and Structural Disorder. *J. Power Sources* **2006**, *156* (2), 655–661. https://doi.org/10.1016/j.jpowsour.2005.05.050.

(4) Li, N.; Bediako, D. K.; Hadt, R. G.; Hayes, D.; Kempa, T. J.; Cube, F. von; Bell, D. C.; Chen, L. X.; Nocera, D. G. Influence of Iron Doping on Tetravalent Nickel Content in Catalytic Oxygen Evolving Films. *Proc. Natl. Acad. Sci. U.S.A.* **2017**, *114* (7), 1486–1491. https://doi.org/10.1073/pnas.1620787114.

(5) Li, N.; Keane, T. P.; Veroneau, S. S.; Hadt, R. G.; Hayes, D.; Chen, L. X.; Nocera, D. G. Template-Stabilized Oxidic Nickel Oxygen Evolution Catalysts. *Proc. Natl. Acad. Sci. U.S.A.* **2020**, 202001529–202001529. https://doi.org/10.1073/pnas.2001529117.

(6) Zou, C.; Li, Z.; Wang, C.; Hong, J.; Chen, J.; Zhong, S. Facile Electrodeposition Route for the Fabrication of Ni/Ni(OH)2 Nanocomposite Films with Different Supporting Electrolytes and Their Electrochemical Properties. *Chem. Phys. Lett.* **2022**, *793*, 139471. https://doi.org/10.1016/j.cplett.2022.139471.

(7) Batchellor, A. S.; Boettcher, S. W. Pulse-Electrodeposited Ni–Fe (Oxy)Hydroxide Oxygen Evolution Electrocatalysts with High Geometric and Intrinsic Activities at Large Mass Loadings. *ACS Catal.* **2015**, *5* (11), 6680–6689. https://doi.org/10.1021/acscatal.5b01551.

(8) Stevens, M. B.; Trang, C. D. M.; Enman, L. J.; Deng, J.; Boettcher, S. W. Reactive Fe-Sites in Ni/Fe (Oxy)Hydroxide Are Responsible for Exceptional Oxygen Electrocatalysis Activity. *J. Am. Chem. Soc.* **2017**, *139* (33), 11361–11364. https://doi.org/10.1021/jacs.7b07117.

(9) Lu, X.; Zhao, C. Electrodeposition of Hierarchically Structured Three-Dimensional Nickel–Iron Electrodes for Efficient Oxygen Evolution at High Current Densities. *Nat Commun* **2015**, *6* (1), 6616. https://doi.org/10.1038/ncomms7616.

(10) Smith, R. D. L.; Pasquini, C.; Loos, S.; Chernev, P.; Klingan, K.; Kubella, P.; Mohammadi, M. R.; González-Flores, D.; Dau, H. Geometric Distortions in Nickel (Oxy)Hydroxide Electrocatalysts by Redox Inactive Iron Ions. *Energy Environ. Sci.* **2018**, *11* (9), 2476–2485. https://doi.org/10.1039/c8ee01063c.

(11) Smith, R. D. L.; Prévot, M. S.; Fagan, R. D.; Zhang, Z.; Sedach, P. A.; Siu, M. K. J.; Trudel, S.; Berlinguette, C. P. Photochemical Route for Accessing Amorphous Metal Oxide Materials for Water Oxidation Catalysis. *Science* **2013**, *340* (6128), 60–63. https://doi.org/10.1126/science.1233638.

(12) Smith, R. D. L.; Prévot, M. S.; Fagan, R. D.; Trudel, S.; Berlinguette, C. P. Water Oxidation Catalysis: Electrocatalytic Response to Metal Stoichiometry in Amorphous Metal Oxide Films Containing Iron, Cobalt, and Nickel. *J. Am. Chem. Soc.* **2013**, *135* (31), 11580–11586. https://doi.org/10.1021/ja403102j.

(13) Alsaç, E. P.; Whittingham, A.; Liu, Y.; Smith, R. D. L. Probing the Role of Internalized Geometric Strain on Heterogeneous Electrocatalysis. *Chem. Mater.* **2019**, *31* (18), 7522–7530. https://doi.org/10.1021/acs.chemmater.9b02234.
(14) Schäfer, H.; Sadaf, S.; Walder, L.; Kuepper, K.; Dinklage, S.; Wollschläger, J.; Schneider, L.; Steinhart, M.; Hardege, J.; Daum, D. Stainless Steel Made to Rust: A Robust Water-Splitting Catalyst with Benchmark Characteristics. *Energy Environ. Sci.* **2015**, *8* (9), 2685–2697. https://doi.org/10.1039/C5EE01601K.
(15) Yamada, N.; Kitano, S.; Yato, Y.; Kowalski, D.; Aoki, Y.; Habazaki, H. In Situ Activation of Anodized Ni–Fe Alloys for the Oxygen Evolution Reaction in Alkaline Media. *ACS Appl. Energy Mater.* **2020**, *3* (12), 12316–12326. https://doi.org/10.1021/acsaem.0c02362.
(16) Fan, J.; Chen, Z.; Shi, H.; Zhao, G. In Situ Grown, Self-Supported Iron–Cobalt–Nickel Alloy Amorphous Oxide Nanosheets with Low Overpotential toward Water Oxidation. *Chem. Commun.* **2016**, *52* (23), 4290–4293. https://doi.org/10.1039/C5CC09699E.
(17) Hibino, T.; Ohya, H. Synthesis of Crystalline Layered Double Hydroxides: Precipitation by Using Urea Hydrolysis and Subsequent Hydrothermal Reactions in Aqueous Solutions. *Appl. Clay Sci.* **2009**, *45* (3), 123–132. https://doi.org/10.1016/j.clay.2009.04.013.
(18) Zhang, C.; Shao, M.; Zhou, L.; Li, Z.; Xiao, K.; Wei, M. Hierarchical NiFe Layered Double Hydroxide Hollow Microspheres with Highly-Efficient Behavior toward Oxygen Evolution Reaction. *ACS Appl. Mater. Interfaces* **2016**, *8* (49), 33697–33703. https://doi.org/10.1021/acsami.6b12100.
(19) Dresp, S.; Luo, F.; Schmack, R.; Kühl, S.; Gliech, M.; Strasser, P. An Efficient Bifunctional Two-Component Catalyst for Oxygen Reduction and Oxygen Evolution in Reversible Fuel Cells, Electrolyzers and Rechargeable Air Electrodes. *Energy Environ. Sci.* **2016**, *9* (6), 2020–2024. https://doi.org/10.1039/C6EE01046F.
(20) Ma, R.; Liu, Z.; Li, L.; Iyi, N.; Sasaki, T. Exfoliating Layered Double Hydroxides in Formamide: A Method to Obtain Positively Charged Nanosheets. *J. Mater. Chem.* **2006**, *16* (39), 3809–3813. https://doi.org/10.1039/b605422f.
(21) Song, F.; Hu, X. Exfoliation of Layered Double Hydroxides for Enhanced Oxygen Evolution Catalysis. *Nat Commun* **2014**, *5* (1), 4477. https://doi.org/10.1038/ncomms5477.
(22) Gicha, B. B.; Tufa, L. T.; Choi, Y.; Lee, J. Amorphous $Ni_{1-x}Fe_x$ Oxyhydroxide Nanosheets with Integrated Bulk and Surface Iron for a High and Stable Oxygen Evolution Reaction. *ACS Appl. Energy Mater.* **2021**, *4* (7), 6833–6841. https://doi.org/10.1021/acsaem.1c00955.
(23) Song, Y.; Xu, B.; Liao, T.; Guo, J.; Wu, Y.; Sun, Z. Electronic Structure Tuning of 2D Metal (Hydr)Oxides Nanosheets for Electrocatalysis. *Small* **2021**, *17* (9), 2002240. https://doi.org/10.1002/smll.202002240.
(24) Zhang, Z.; Zhou, D.; Liao, J.; Bao, X.; Yu, H. Synthesis of High Crystalline Nickel-Iron Hydrotalcite-like Compound as an Efficient Electrocatalyst for Oxygen Evolution Reaction. *Int. J. Energy Res.* **2019**, *43* (4), 1460–1467. https://doi.org/10.1002/er.4359.
(25) Li, R.; Xu, J.; Pan, Q.; Ba, J.; Tang, T.; Luo, W. One-Step Synthesis of NiFe Layered Double Hydroxide Nanosheet Array/N-Doped Graphite Foam Electrodes for Oxygen Evolution Reactions. *ChemistryOpen* **2019**, *8* (7), 1027–1032. https://doi.org/10.1002/open.201900190.
(26) Luo, X.; Wei, X.; Zhong, H.; Wang, H.; Wu, Y.; Wang, Q.; Gu, W.; Gu, M.; Beckman, S. P.; Zhu, C. Single-Atom Ir-Anchored 3D Amorphous NiFe Nanowire@Nanosheets for

Boosted Oxygen Evolution Reaction. *ACS Appl. Mater. Interfaces* **2020**, *12* (3), 3539–3546. https://doi.org/10.1021/acsami.9b17476.
(27) Zhang, J.; Liu, J.; Xi, L.; Yu, Y.; Chen, N.; Sun, S.; Wang, W.; Lange, K. M.; Zhang, B. Single-Atom Au/NiFe Layered Double Hydroxide Electrocatalyst: Probing the Origin of Activity for Oxygen Evolution Reaction. *J. Am. Chem. Soc.* **2018**, *140* (11), 3876–3879. https://doi.org/10.1021/jacs.8b00752.
(28) Zheng, X.; Tang, J.; Gallo, A.; Torres, J. A. G.; Yu, X.; Athanitis, C. J.; Been, E. M.; Ercius, P.; Mao, H.; Fakra, S. C.; Song, C.; Davis, R. C.; Reimer, J. A.; Vinson, J.; Bajdich, M.; Cui, Y. Origin of Enhanced Water Oxidation Activity in an Iridium Single Atom Anchored on NiFe Oxyhydroxide Catalyst. *Proc. Natl. Acad. Sci. U.S.A.* **2021**, *118* (36), e2101817118. https://doi.org/10.1073/pnas.2101817118.
(29) Rinawati, M.; Wang, Y.-X.; Chen, K.-Y.; Yeh, M.-H. Designing a Spontaneously Deriving NiFe-LDH from Bimetallic MOF-74 as an Electrocatalyst for Oxygen Evolution Reaction in Alkaline Solution. *Chem. Eng. J.* **2021**, *423*, 130204. https://doi.org/10.1016/j.cej.2021.130204.
(30) Alsaç, E. P.; Bodappa, N.; Whittingham, A. W. H.; Liu, Y.; de Lazzari, A.; Smith, R. D. L. Structure–Property Correlations for Analysis of Heterogeneous Electrocatalysts. *Chem. Phys. Rev.* **2021**, *2* (3), 031306. https://doi.org/10.1063/5.0058704.
(31) Chen, J. Y. C.; Dang, L.; Liang, H.; Bi, W.; Gerken, J. B.; Jin, S.; Alp, E. E.; Stahl, S. S. Operando Analysis of NiFe and Fe Oxyhydroxide Electrocatalysts for Water Oxidation: Detection of Fe^{4+} by Mössbauer Spectroscopy. *J. Am. Chem. Soc.* **2015**, *137* (48), 15090–15093. https://doi.org/10.1021/jacs.5b10699.
(32) Peng, C.; Ran, N.; Wan, G.; Zhao, W.; Kuang, Z.; Lu, Z.; Sun, C.; Liu, J.; Wang, L.; Chen, H. Engineering Active Fe Sites on Nickel–Iron Layered Double Hydroxide through Component Segregation for Oxygen Evolution Reaction. *ChemSusChem* **2020**, *13* (4), 811–818. https://doi.org/10.1002/cssc.201902841.
(33) Kuai, C.; Xi, C.; Hu, A.; Zhang, Y.; Xu, Z.; Nordlund, D.; Sun, C.-J.; Cadigan, C. A.; Richards, R. M.; Li, L.; Dong, C.-K.; Du, X.-W.; Lin, F. Revealing the Dynamics and Roles of Iron Incorporation in Nickel Hydroxide Water Oxidation Catalysts. *J. Am. Chem. Soc.* **2021**, *143*, 18519–18526. https://doi.org/10.1021/jacs.1c07975.
(34) Zhou, Y.; López, N. The Role of Fe Species on NiOOH in Oxygen Evolution Reactions. *ACS Catal.* **2020**, *10* (11), 6254–6261. https://doi.org/10.1021/acscatal.0c00304.
(35) Hunter, B. M.; Thompson, N. B.; Müller, A. M.; Rossman, G. R.; Hill, M. G.; Winkler, J. R.; Gray, H. B. Trapping an Iron(VI) Water-Splitting Intermediate in Nonaqueous Media. *Joule* **2018**, *2* (4), 747–763. https://doi.org/10.1016/j.joule.2018.01.008.
(36) Steimecke, M.; Seiffarth, G.; Schneemann, C.; Oehler, F.; Förster, S.; Bron, M. Higher-Valent Nickel Oxides with Improved Oxygen Evolution Activity and Stability in Alkaline Media Prepared by High-Temperature Treatment of $Ni(OH)_2$. *ACS Catal.* **2020**, *10* (6), 3595–3603. https://doi.org/10.1021/acscatal.9b04788.
(37) Qiao, C.; Usman, Z.; Cao, T.; Rafai, S.; Wang, Z.; Zhu, Y.; Cao, C.; Zhang, J. High-Valence Ni and Fe Sites on Sulfated NiFe-LDH Nanosheets to Enhance O-O Coupling for Water Oxidation. *Chem. Eng. J.* **2021**, *426*, 130873. https://doi.org/10.1016/j.cej.2021.130873.
(38) Friebel, D.; Louie, M. W.; Bajdich, M.; Sanwald, K. E.; Cai, Y.; Wise, A. M.; Cheng, M. J.; Sokaras, D.; Weng, T. C.; Alonso-Mori, R.; Davis, R. C.; Bargar, J. R.; Nørskov, J. K.; Nilsson, A.; Bell, A. T. Identification of Highly Active Fe Sites in (Ni,Fe)OOH for

Electrocatalytic Water Splitting. *J. Am. Chem. Soc.* **2015**, *137* (3), 1305–1313. https://doi.org/10.1021/ja511559d.
(39) Zeng, Y.; Li, X.; Wang, J.; Sougrati, M. T.; Huang, Y.; Zhang, T.; Liu, B. In Situ/Operando Mössbauer Spectroscopy for Probing Heterogeneous Catalysis. *Chem Catalysis* **2021**, *1* (6), 1215–1233. https://doi.org/10.1016/j.checat.2021.08.013.
(40) Zhou, D.; Li, P.; Lin, X.; McKinley, A.; Kuang, Y.; Liu, W.; Lin, W.-F.; Sun, X.; Duan, X. Layered Double Hydroxide-Based Electrocatalysts for the Oxygen Evolution Reaction: Identification and Tailoring of Active Sites, and Superaerophobic Nanoarray Electrode Assembly. *Chem. Soc. Rev* **2021**, *50* (15), 8790–8817. https://doi.org/10.1039/D1CS00186H.
(41) Anantharaj, S.; Kundu, S.; Noda, S. "The Fe Effect": A Review Unveiling the Critical Roles of Fe in Enhancing OER Activity of Ni and Co Based Catalysts. *Nano Energy* **2021**, *80*, 105514. https://doi.org/10.1016/j.nanoen.2020.105514.
(42) Chen, W.; Wu, B.; Wang, Y.; Zhou, W.; Li, Y.; Liu, T.; Xie, C.; Xu, L.; Du, S.; Song, M.; Wang, D.; Liu, Y.; Li, Y.; Liu, J.; Zou, Y.; Chen, R.; Chen, C.; Zheng, J.; Li, Y.; Chen, J.; Wang, S. Deciphering the Alternating Synergy between Interlayer Pt Single-Atom and NiFe Layered Double Hydroxide for Overall Water Splitting. *Energy Environ. Sci.* **2021**, *14*, 6428–6440. https://doi.org/10.1039/D1EE01395E.
(43) Chung, D. Y.; Lopes, P. P.; Farinazzo Bergamo Dias Martins, P.; He, H.; Kawaguchi, T.; Zapol, P.; You, H.; Tripkovic, D.; Strmcnik, D.; Zhu, Y.; Seifert, S.; Lee, S.; Stamenkovic, V. R.; Markovic, N. M. Dynamic Stability of Active Sites in Hydr(Oxy)Oxides for the Oxygen Evolution Reaction. *Nat Energy* **2020**, *5* (3), 222–230. https://doi.org/10.1038/s41560-020-0576-y.
(44) Gourrier, L.; Deabate, S.; Michel, T.; Paillet, M.; Hermet, P.; Bantignies, J.-L.; Henn, F. Characterization of Unusually Large "Pseudo-Single Crystal" of β-Nickel Hydroxide. *J. Phys. Chem. C* **2011**, *115* (30), 15067–15074. https://doi.org/10.1021/jp203222t.
(45) Bediako, D. K.; Surendranath, Y.; Nocera, D. G. Mechanistic Studies of the Oxygen Evolution Reaction Mediated by a Nickel–Borate Thin Film Electrocatalyst. *J. Am. Chem. Soc.* **2013**, *135* (9), 3662–3674. https://doi.org/10.1021/ja3126432.
(46) Ma, K.; Cheng, J. P.; Zhang, J.; Li, M.; Liu, F.; Zhang, X. Dependence of Co/Fe Ratios in Co-Fe Layered Double Hydroxides on the Structure and Capacitive Properties. *Electrochim. Acta* **2016**, *198*, 231–240. https://doi.org/10.1016/j.electacta.2016.03.082.
(47) Krehula, S.; Ristić, M.; Wu, C.; Li, X.; Jiang, L.; Wang, J.; Sun, G.; Zhang, T.; Perović, M.; Bošković, M.; Antić, B.; Krehula, L. K.; Kobzi, B.; Kubuki, S.; Musić, S. Influence of Fe(III) Doping on the Crystal Structure and Properties of Hydrothermally Prepared β-Ni(OH)2 Nanostructures. *J. Alloys Compd.* **2018**, *750*, 687–695. https://doi.org/10.1016/j.jallcom.2018.04.032.
(48) Sun, Y.; Zhou, Y.; Wang, Z.; Ye, X. Structural and Morphological Transformations of Zn–Al Layered Double Hydroxides through Hydrothermal Treatment. *Appl. Surf. Sci.* **2009**, *255* (12), 6372–6377. https://doi.org/10.1016/j.apsusc.2009.02.018.
(49) Abellán, G.; Carrasco, J. A.; Coronado, E. Room Temperature Magnetism in Layered Double Hydroxides Due to Magnetic Nanoparticles. *Inorg. Chem.* **2013**, *52* (14), 7828–7830. https://doi.org/10.1021/ic400883k.
(50) Abellán, G.; Coronado, E.; Martí-Gastaldo, C.; Pinilla-Cienfuegos, E.; Ribera, A. Hexagonal Nanosheets from the Exfoliation of Ni^{2+}−Fe^{3+} LDHs: A Route towards Layered

Multifunctional Materials. *J. Mater. Chem.* **2010**, *20* (35), 7451–7455. https://doi.org/10.1039/C0JM01447H.
(51) Han, Y.; Liu, Z.-H.; Yang, Z.; Wang, Z.; Tang, X.; Wang, T.; Fan, L.; Ooi, K. Preparation of Ni^{2+}−Fe^{3+} Layered Double Hydroxide Material with High Crystallinity and Well-Defined Hexagonal Shapes. *Chem. Mater.* **2008**, *20* (2), 360–363. https://doi.org/10.1021/cm7023789.
(52) Yu, J.; Liu, J.; Clearfield, A.; Sims, J. E.; Speiegle, M. T.; Suib, S. L.; Sun, L. Synthesis of Layered Double Hydroxide Single-Layer Nanosheets in Formamide. *Inorg. Chem.* **2016**, *55* (22), 12036–12041. https://doi.org/10.1021/acs.inorgchem.6b02203.
(53) Alsaç, E. P.; Zhou, K.; Rong, W.; Salamon, S.; Landers, J.; Wende, H.; Smith, R. D. L. Identification of Non-Traditional Coordination Environments for Iron Ions in Nickel Hydroxide Lattices. *Energy Environ. Sci.* **2022**, *15*, 2638–2652. https://doi.org/10.1039/D2EE00396A.
(54) Hall, D. S.; Lockwood, D. J.; Bock, C.; MacDougall, B. R. Nickel Hydroxides and Related Materials: A Review of Their Structures, Synthesis and Properties. *Proc. R. Soc. A* **2014**, *471*, 20140792.
(55) Kazimirov, V. Yu.; Smirnov, M. B.; Bourgeois, L.; Guerlou-Demourgues, L.; Servant, L.; Balagurov, A. M.; Natkaniec, I.; Khasanova, N. R.; Antipov, E. V. Atomic Structure and Lattice Dynamics of Ni and Mg Hydroxides. *Solid State Ion.* **2010**, *181* (39), 1764–1770. https://doi.org/10.1016/j.ssi.2010.10.002.
(56) Yew, Y. P.; Shameli, K.; Miyake, M.; Kuwano, N.; Bt Ahmad Khairudin, N. B.; Bt Mohamad, S. E.; Lee, K. X. Green Synthesis of Magnetite (Fe_3O_4) Nanoparticles Using Seaweed (Kappaphycus Alvarezii) Extract. *Nanoscale Res. Lett* **2016**, *11* (1), 276. https://doi.org/10.1186/s11671-016-1498-2.
(57) Singh, M.; Ulbrich, P.; Prokopec, V.; Svoboda, P.; Šantavá, E.; Štěpánek, F. Vapour Phase Approach for Iron Oxide Nanoparticle Synthesis from Solid Precursors. *J. Solid State Chem.* **2013**, *200*, 150–156. https://doi.org/10.1016/j.jssc.2013.01.037.
(58) Hall, D. S.; Lockwood, D. J.; Poirier, S.; Bock, C.; MacDougall, B. R. Raman and Infrared Spectroscopy of α and β Phases of Thin Nickel Hydroxide Films Electrochemically Formed on Nickel. *J. Phys. Chem. A* **2012**, *116* (25), 6771–6784. https://doi.org/10.1021/jp303546r.
(59) Bantignies, J. L.; Deabate, S.; Righi, A.; Rols, S.; Hermet, P.; Sauvajol, J. L.; Henn, F. New Insight into the Vibrational Behavior of Nickel Hydroxide and Oxyhydroxide Using Inelastic Neutron Scattering, Far/Mid-Infrared and Raman Spectroscopies. *J. Phys. Chem. C* **2008**, *112* (6), 2193–2201. https://doi.org/10.1021/jp075819e.
(60) Ishikawa, T.; Matsumoto, K.; Kandori, K.; Nakayama, T. Synthesis of Layered Zinc Hydroxide Chlorides in the Presence of Al(III). *J. Solid State Chem.* **2006**, *179* (4), 1110–1118. https://doi.org/10.1016/j.jssc.2006.01.007.
(61) Deabate, S.; Fourgeot, F.; Henn, F. X-Ray Diffraction and Micro-Raman Spectroscopy Analysis of New Nickel Hydroxide Obtained by Electrodialysis. *J. Power Sources* **2000**, *87* (1), 125–136. https://doi.org/10.1016/S0378-7753(99)00437-1.
(62) Hanesch, M. Raman Spectroscopy of Iron Oxides and (Oxy)Hydroxides at Low Laser Power and Possible Applications in Environmental Magnetic Studies. *Geophys. J. Int.* **2009**, *177* (3), 941–948. https://doi.org/10.1111/j.1365-246X.2009.04122.x.
(63) Chourpa, I.; Douziech-Eyrolles, L.; Ngaboni-Okassa, L.; Fouquenet, J. F.; Cohen-Jonathan, S.; Soucé, M.; Marchais, H.; Dubois, P. Molecular Composition of Iron Oxide

Nanoparticles, Precursors for Magnetic Drug Targeting, as Characterized by Confocal Raman Microspectroscopy. *Analyst* **2005**, *130* (10), 1395–1403. https://doi.org/10.1039/b419004a.

(64) Westre, T. E.; Kennepohl, P.; DeWitt, J. G.; Hedman, B.; Hodgson, K. O.; Solomon, E. I. A Multiplet Analysis of Fe K-Edge 1s → 3d Pre-Edge Features of Iron Complexes. *J. Am. Chem. Soc.* **1997**, *119* (27), 6297–6314. https://doi.org/10.1021/ja964352a.

(65) Yamamoto, T. Assignment of Pre-Edge Peaks in K-Edge X-Ray Absorption Spectra of 3d Transition Metal Compounds: Electric Dipole or Quadrupole? *X-Ray Spectrom.* **2008**, *37* (6), 572–584. https://doi.org/10.1002/xrs.1103.

(66) Boubnov, A.; Lichtenberg, H.; Mangold, S.; Grunwaldt, J.-D. Identification of the Iron Oxidation State and Coordination Geometry in Iron Oxide- and Zeolite-Based Catalysts Using Pre-Edge XAS Analysis. *J Synchrotron Rad* **2015**, *22* (2), 410–426. https://doi.org/10.1107/S1600577514025880.

(67) Wilke, M.; Farges, F.; Petit, P.-E.; Brown, G. E.; Martin, F. Oxidation State and Coordination of Fe in Minerals: An Fe *K*- XANES Spectroscopic Study. *Am. Mineral.* **2001**, *86* (5–6), 714–730. https://doi.org/10.2138/am-2001-5-612.

(68) Xia, Z.; Zhang, H.; Shen, K.; Qu, Y.; Jiang, Z. Wavelet Analysis of Extended X-Ray Absorption Fine Structure Data: Theory, Application. *Phys. B: Condens. Matter.* **2018**, *542*, 12–19. https://doi.org/10.1016/j.physb.2018.04.039.

(69) Funke, H.; Chukalina, M.; Scheinost, A. C. A New FEFF-Based Wavelet for EXAFS Data Analysis. *J Synchrotron Rad* **2007**, *14* (5), 426–432. https://doi.org/10.1107/S0909049507031901.

(70) Wang, S.; Nai, J.; Yang, S.; Guo, L. Synthesis of Amorphous Ni−Zn Double Hydroxide Nanocages with Excellent Electrocatalytic Activity toward Oxygen Evolution Reaction. *ChemNanoMat* **2015**, *1* (5), 324–330. https://doi.org/10.1002/cnma.201500067.

(71) Farhat, R.; Dhainy, J.; Halaoui, L. I. OER Catalysis at Activated and Codeposited NiFe-Oxo/Hydroxide Thin Films Is Due to Postdeposition Surface-Fe and Is Not Sustainable without Fe in Solution. *ACS Catal.* **2020**, *10* (1), 20–35. https://doi.org/10.1021/acscatal.9b02580.

(72) Görlin, M.; Chernev, P.; Paciok, P.; Tai, C. W.; Ferreira de Araújo, J.; Reier, T.; Heggen, M.; Dunin-Borkowski, R.; Strasser, P.; Dau, H. Formation of Unexpectedly Active Ni-Fe Oxygen Evolution Electrocatalysts by Physically Mixing Ni and Fe Oxyhydroxides. *Chem. Commun.* **2019**, *55* (6), 818–821. https://doi.org/10.1039/c8cc06410e.

(73) Shebanova, O. N.; Lazor, P. Raman Spectroscopic Study of Magnetite ($FeFe_2O_4$): A New Assignment for the Vibrational Spectrum. *J. Solid State Chem.* **2003**, *174* (2), 424–430. https://doi.org/10.1016/S0022-4596(03)00294-9.

(74) Peng, L.; Yang, N.; Yang, Y.; Wang, Q.; Xie, X.; Sun-Waterhouse, D.; Shang, L.; Zhang, T.; Waterhouse, G. I. N. Atomic Cation-Vacancy Engineering of NiFe-Layered Double Hydroxides for Improved Activity and Stability towards the Oxygen Evolution Reaction. *Angew.Chem.Int.Ed* **2021**, *133* (46), 24817–24824. https://doi.org/10.1002/ange.202109938.

(75) Kumaravel, S.; Karthick, K.; Sankar, S. S.; Karmakar, A.; Madhu, R.; Bera, K.; Kundu, S. Current Progressions in Transition Metal Based Hydroxides as Bi-Functional Catalysts towards Electrocatalytic Total Water Splitting. *Sustain. Energy Fuels* **2021**, *5* (24), 6215–6268. https://doi.org/10.1039/D1SE01193F.

(76) Görlin, M.; Chernev, P.; De Araújo, J. F.; Reier, T.; Dresp, S.; Paul, B.; Krähnert, R.; Dau, H.; Strasser, P. Oxygen Evolution Reaction Dynamics, Faradaic Charge Efficiency, and the Active Metal Redox States of Ni-Fe Oxide Water Splitting Electrocatalysts. *J. Am. Chem. Soc.* **2016**, *138* (17), 5603–5614. https://doi.org/10.1021/jacs.6b00332.
(77) Kuai, C.; Xu, Z.; Xi, C.; Hu, A.; Yang, Z.; Zhang, Y.; Sun, C.-J.; Li, L.; Sokaras, D.; Dong, C.; Qiao, S.-Z.; Du, X.-W.; Lin, F. Phase Segregation Reversibility in Mixed-Metal Hydroxide Water Oxidation Catalysts. *Nat Catal* **2020**, *3* (9), 743–753. https://doi.org/10.1038/s41929-020-0496-z.
(78) Dionigi, F.; Zhu, J.; Zeng, Z.; Merzdorf, T.; Sarodnik, H.; Gliech, M.; Pan, L.; Li, W.-X.; Greeley, J.; Strasser, P. Intrinsic Electrocatalytic Activity for Oxygen Evolution of Crystalline 3d-Transition Metal Layered Double Hydroxides. *Angew.Chem.Int.Ed* **2021**, *60* (26), 14446–14457. https://doi.org/10.1002/anie.202100631.
(79) Corrigan, D. A. The Catalysis of the Oxygen Evolution Reaction by Iron Impurities in Thin Film Nickel Oxide Electrodes. *J. Electrochem. Soc.* **1987**, *134* (2), 377–377. https://doi.org/10.1149/1.2100463.
(80) Trotochaud, L.; Young, S. L.; Ranney, J. K.; Boettcher, S. W. Nickel-Iron Oxyhydroxide Oxygen-Evolution Electrocatalysts: The Role of Intentional and Incidental Iron Incorporation. *J. Am. Chem. Soc.* **2014**, *136* (18), 6744–6753. https://doi.org/10.1021/ja502379c.
(81) Bockris, J. O. Kinetics of Activation Controlled Consecutive Electrochemical Reactions: Anodic Evolution of Oxygen. *J. Chem. Phys.* **1956**, *24* (1956), 817–817. https://doi.org/10.1063/1.1742616.
(82) Bockris, J. O.; Otagawa, T. Mechanism of Oxygen Evolution on Perovskites. *J. Phys. Chem.* **1983**, *57*, 2960–2971.
(83) Shinagawa, T.; Garcia-Esparza, A. T.; Takanabe, K. Insight on Tafel Slopes from a Microkinetic Analysis of Aqueous Electrocatalysis for Energy Conversion. *Sci. Rep.* **2015**, *5*, 13801–13801. https://doi.org/10.1038/srep13801.
(84) Laborda, E.; Henstridge, M. C.; Compton, R. G. Asymmetric Marcus Theory: Application to Electrode Kinetics. *J. Electroanal. Chem.* **2012**, *667*, 48–53. https://doi.org/10.1016/j.jelechem.2011.12.011.
(85) Li, D.; Lin, C.; Batchelor-McAuley, C.; Chen, L.; Compton, R. G. Tafel Analysis in Practice. *J. Electroanal. Chem.* **2018**, *826*, 117–124. https://doi.org/10.1016/j.jelechem.2018.08.018.
(86) Henstridge, M. C.; Rees, N. V.; Compton, R. G. A Comparison of the Butler–Volmer and Asymmetric Marcus–Hush Models of Electrode Kinetics at the Channel Electrode. *J. Electroanal. Chem.* **2012**, *687*, 79–83. https://doi.org/10.1016/j.jelechem.2012.10.012.
(87) Henstridge, M. C.; Laborda, E.; Compton, R. G. Asymmetric Marcus–Hush Model of Electron Transfer Kinetics: Application to the Voltammetry of Surface-Bound Redox Systems. *J. Electroanal. Chem.* **2012**, *674*, 90–96. https://doi.org/10.1016/j.jelechem.2012.04.006.
(88) Laborda, E.; C. Henstridge, M.; Batchelor-McAuley, C.; G. Compton, R. Asymmetric Marcus–Hush Theory for Voltammetry. *Chem. Soc. Rev* **2013**, *42* (12), 4894–4905. https://doi.org/10.1039/C3CS35487C.
(89) Henstridge, M. C.; Laborda, E.; Rees, N. V.; Compton, R. G. Marcus–Hush–Chidsey Theory of Electron Transfer Applied to Voltammetry: A Review. *Electrochim. Acta* **2012**, *84*, 12–20. https://doi.org/10.1016/j.electacta.2011.10.026.

(90) Miao, Y.; Zhao, Y.; Zhang, S.; Shi, R.; Zhang, T. Strain Engineering: A Boosting Strategy for Photocatalysis. *Adv. Mater.* **2022**, *34* (29), 2200868. https://doi.org/10.1002/adma.202200868.
(91) You, B.; Tang, M. T.; Tsai, C.; Abild-Pedersen, F.; Zheng, X.; Li, H. Enhancing Electrocatalytic Water Splitting by Strain Engineering. *Adv. Mater.* **2019**, *31* (17), 1807001. https://doi.org/10.1002/adma.201807001.
(92) Goldsmith, Z. K.; Harshan, A. K.; Gerken, J. B.; Vörös, M.; Galli, G.; Stahl, S. S.; Hammes-Schiffer, S. Characterization of NiFe Oxyhydroxide Electrocatalysts by Integrated Electronic Structure Calculations and Spectroelectrochemistry. *Proc. Natl. Acad. Sci. U.S.A.* **2017**, *114* (12), 3050–3055. https://doi.org/10.1073/pnas.1702081114.
(93) Ravel, B.; Newville, M. ATHENA, ARTEMIS, HEPHAESTUS: Data Analysis for X-Ray Absorption Spectroscopy Using IFEFFIT. *J Synchrotron Rad* **2005**, *12* (4), 537–541. https://doi.org/10.1107/S0909049505012719.
(94) Funke, H.; Scheinost, A. C.; Chukalina, M. Wavelet Analysis of Extended X-Ray Absorption Fine Structure Data. *Phys. Rev. B* **2005**, *71* (9), 094110. https://doi.org/10.1103/PhysRevB.71.094110.
(95) Siebecker, M. G.; Sparks, D. L. Structural Differentiation between Layered Single (Ni) and Double Metal Hydroxides (Ni–Al LDHs) Using Wavelet Transformation. *J. Phys. Chem. A* **2017**, *121* (37), 6992–6999. https://doi.org/10.1021/acs.jpca.7b07940.

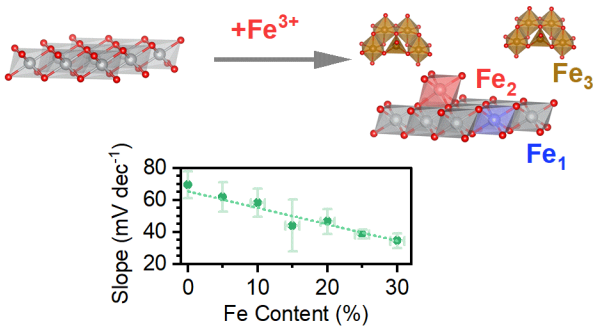
+Fe3+
Fe2
Fe3
Fe1
Slope (mV dec-1)
80
60
40
20
0
10
20
30
Fe Content (%)